QUANTUM ELECTRON OPTICS AND ITS APPLICATIONS

W. D. OLIVER, R. C. LIU, J. KIM, X. MAITRE, L. DI CARLO AND Y. YAMAMOTO
Departments of Electrical Engineering and Applied Physics
Ginzton Laboratory, Stanford, CA 94305

1. Introduction

With the development of two-dimensional electron gas (2DEG) substrates and submicron lithography techniques, it has become possible to fabricate mesoscopic devices with length scales smaller than the inelastic and elastic scattering lengths of electrons at cryogenic temperatures. In these ballistic devices, the wave-nature of the electron can be probed through dc conductance measurements, proportional to the first-order correlation function of the wavefunction amplitude. Electron focussing, diffraction, and Aharonov-Bohm interference experiments are examples of classical optical phenomena clearly observed in mesoscopic electron systems [1].

The study of higher-order correlation functions, or *quantum optical* phenomena, of electrons and composite particles in mesoscopic systems opens the field of quantum electron optics. Identical quantum particles are inherently indistinguishable, and this oftentimes leads to non-classical behaviors manifest in higher-order correlation functions. Since the 1950's, probing higher-order correlation functions in photon and atom-cavity systems has led to a more complete understanding of fundamental quantum statistical [2, 3] and quantum mechanical phenomena resulting from entanglement [4–6], including violations of Bell's inequality [7–9], quantum nondemolition measurements [10, 11], and teleportation [12–14]. Recent experiments have demonstrated that quantum optical effects can also be observed clearly in mesoscopic electron systems [15–21].

In this paper, we present two recent experiments that use current fluctuation measurements to probe the second-order electron correlation function (fourth-order in wavefunction amplitude): an intensity interferometry experiment called the Hanbury Brown and Twiss (HBT) experiment [2, 21],

and an electron collision experiment [19]. Finally, we discuss how these two experiments can be used to characterize the unique behavior of Bell's state entangled electrons in a proposed electron bunching experiment [22–24]. Throughout the paper, we consider only ballistic systems, in which the inelastic phonon scattering and the elastic ionized impurity scattering lengths are much longer than the characteristic size of the system at cryogenic temperatures (typically 1.5K in our experiments). The screening length (typically $\lambda_{sc} \approx 5$ nm) is assumed to be much smaller than the Fermi wavelength (typically $\lambda_F \approx 40$ nm) so that Coulomb interactions can be neglected. We assume ideal thermal reservoirs, independent transport channels, and transmission probabilities independent of the applied bias voltage. This approach directly follows the coherent scattering formalism [25, 26].

2. Equilibrium and Non-equilibrium Noise

There are three primary contributions to the noise in the mesoscopic systems considered here: thermal reservoir, single-particle partition, and two-particle collision noise. At thermal equilibrium, a reservoir exhibits noise due to the quantum statistical nature in which particles occupy an available mode [25, 26]. In a thermal boson reservoir, additional particles are emitted into a given mode through a spontaneous and stimulated emission process yielding particle number fluctuations $\langle \Delta {N_k}^2 \rangle_B = \langle N_k \rangle (1 + \langle N_k \rangle)$, where $\langle N_k \rangle = f_B(E_k)$ is the Bose-Einstein distribution [2]. A thermal fermion reservoir will emit particles into a given mode through a phase-space filling process, a manifestation of the Pauli exclusion principle, yielding $\langle \Delta {N_k}^2 \rangle_F = \langle N_k \rangle (1 - \langle N_k \rangle)$ where $\langle N_k \rangle = f_F(E_k)$ is the Fermi-Dirac distribution [27]. In the low-degeneracy limit, $\langle N_k \rangle \ll 1$, both fermions and bosons carry Poisson-like statistics, $\langle \Delta {N_k}^2 \rangle \approx \langle N_k \rangle$. Since many classical phenomena also carry Poisson-like statistics, it is convenient to use Poisson statistics as a reference point to characterize noise processes. We define the Fano factor, $F = \langle \Delta {N_k}^2 \rangle / \langle N_k \rangle$, where $F_C = 1$ (Poisson distributed noise) for a classical reservoir, $F_B = 1 + \langle N_k \rangle > 1$ (super-Poisson distributed noise) for a thermal boson reservoir, and $F_F = 1 - \langle N_k \rangle$, $0 \leq F_F < 1$ (sub-Poisson distributed noise) for a thermal fermion reservoir.

Under non-equilibrium conditions when there is a net flux of particles from a source, partition noise can arise due to the random deletion of the input flux and is fundamentally a single-particle effect. Non-equilibrium collision noise, fundamentally a two-particle effect, is discussed in section 4. In figure 1a, we consider the partitioning of particles from a source with Fano factor F_1 at a beam splitter with transmission probability T. The average number of particles transmitted to output 3 is $\langle N_3 \rangle = T \langle N_1 \rangle$. The

variance in particle number at output 3 is given by the Burgess variance theorem, $\langle \Delta N_3^2 \rangle = \langle \Delta N_1^2 \rangle T^2 + \langle N_1 \rangle T(1-T)$ in which the first term is the attenuated source noise and the second term is the partition noise [28]. It follows that the Fano factor at output 3 is $F_3 = TF_1 + (1-T)$. Note that this mesoscopic beamsplitter also models a single channel through a quantum point contact (QPC). Between the $(n-1)$ and n'th conductance plateau, there are $(n-1)$ channels (beamsplitters) transmitting with unity probability, and the n'th channel (beamsplitter) transmitting with probability T_n (all beamsplitters in parallel). In this case, for a quiet source ($F_1 = 0$), it can be shown that ${F_3}^{(n)} = T_n(1-T_n)/[T_n + (n-1)]$ at the output of the n-channel QPC [15, 16, 19].

3. Hanbury Brown and Twiss-type Intensity Interferometer

In principle, one can measure the current noise of a particle source (reservoir, beamsplitter, QPC, *etc.,*) by placing a noise detector immediately after it. This is usually done in mesoscopic systems using a square-law device followed by an averager to get a quantity proportional to the time average of the squared current. However, a careful calibration is needed to interpret the resulting value, because the transfer function accounting for the noise detection circuit is usually not known *a priori*. One possibility is to put a known noise source in parallel with one's device, but this may hamper the operation of the device. Another possibility is to characterize the detection system without the device, but then adding the device later may change the transfer function.

Another approach is to physically place a beamsplitter after the noise source and calculate the cross-covariance of the output fluxes as shown in figure 1a. The normalized cross-covariance is defined as

$$\rho(\tau) = \frac{\langle \Delta N_2(t) \Delta N_3(t+\tau) \rangle}{\langle \Delta N_2^2 \rangle^{\frac{1}{2}} \langle \Delta N_3^2 \rangle^{\frac{1}{2}}}, \tag{1}$$

where τ is the relative delay time between the beamsplitter outputs. By definition, this is the cross-correlation of the output fluctuations ΔN_2 and ΔN_3. One can uniquely determine the Fano factor of a noise source from the cross-covariance for a $T = 0.5$ beamsplitter with zero delay, $\rho(\tau = 0) = (F_1 - 1)/(F_1 + 1)$. In this case, the cross-covariance is positive for $F_1 > 1$ (super-Poisson distributed noise), negative for $0 \leq F_1 < 1$ (sub-Poisson distributed noise), and zero for $F_1 = 1$ (classical, Poisson distributed noise). The advantage of this approach is that, for matched electronics between the two outputs, the transfer function of the experimental detection system is normalized out of the expression. The positive cross-covariance for photons from a thermal photon reservoir was demonstrated

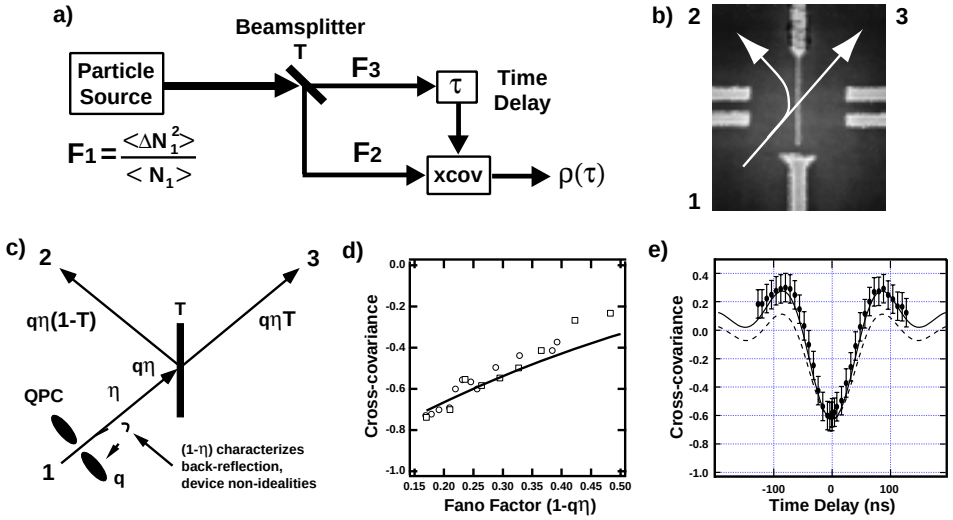

Figure 1. a) Cross-covariance schematic. The Fano factor of the source, F_1, can be determined from the cross-covariance, $\rho(\tau)$. b) Device used for the HBT-type intensity interferometer for electrons. Arrows indicate electron entry and partitioning at the electron beamsplitter. c) Probability model for HBT-type intensity interferometer. q is the QPC transmission probability, η accounts for device non-idealities, and T is the beamsplitter transmission probability. d) Cross-covariance *vs.* input Fano factor with $T \approx 0.5$ and $\eta \approx 0.83$. The cross-covariance decreases towards -1 as the Fano factor is reduced towards zero, indicating a quiet source. The solid line is a theoretical trace using equation 2. e) Cross-covariance *vs.* delay time at $F = 0.23$. The cross-covariance features a sinc-like behavior due to the finite detection bandwidth (2-10 MHz). A simulation yields the solid line for the actual 2-10 MHz bandwidth, while the dotted line represents a 0-10 MHz lowpass configuration for comparison.

more than forty years ago by Hanbury Brown and Twiss [2]. This intensity interferometry technique has subsequently become an important tool for probing the statistics of photons generated by various types of sources [29–31].

We recently demonstrated intensity interferometry with electrons in a 2DEG system shown in figure 1b [21]. Schottky gates and an etched trench define a four-port device with a narrow, tunable electron beamsplitter. An equivalent transmission probability model is shown in figure 1c. The QPC serves as the Fermi-degenerate, single-mode, electron source. In this model, the QPC is ideal with transmission probability $q \in [0, 1]$. Non-idealities, such as coherent back-reflection from the electron beamsplitter, are characterized by the conditional transmission probability, η, which can be experimentally determined. Using this probability model, one can derive an

analytic expression for the cross-covariance,

$$\rho(\tau=0) = \frac{F-1}{\sqrt{F+\frac{T}{1-T}}\sqrt{F+\frac{1-T}{T}}} = -\left[\frac{q\eta T \cdot q\eta \bar{T}}{(1-q\eta T)(1-q\eta \bar{T})}\right]^{\frac{1}{2}} \quad (2)$$

where $F = (1-q\eta)$ is the Fano factor of the source (including the reservoir, QPC transmission probability, and losses) as seen from the beamsplitter, and $\bar{T} \equiv (1-T)$. Experimentally, one can vary the Fano factor of the source, F, by tuning the QPC transmission probability, q. The cross-covariance as a function of the Fano factor is plotted in figure 1d. As the transmission, q, through the QPC is increased, the Fano factor, F, is decreased, and the input electron flux to the beam splitter carries less (current-normalized) noise. The experimental cross-covariance coefficient approaches -1 as F decreases, in close agreement with the analytical trace calculated using equation 2. Figure 1e shows the cross-covariance as a function of the relative delay time, τ, between the two output arms for $F = 0.23$. The sinc-like oscillatory behavior and side-lobe dc-offset are due to the detection bandwidth of our measurement system, 2-10 MHz. The solid line is a zero-parameter fit from a simulation which accounts for the actual detection system including this bandwidth. For comparison, the dashed line is from a simulation using a low pass bandwidth 0-10 MHz which removes the side-lobe dc-offset.

4. Quantum Interference in Electron Collision

The Hanbury Brown and Twiss-type intensity interferometry experiment is a useful tool to probe the noise of a given system. If that system is known to be a degenerate thermal reservoir, then one can also conclude the type of particle, fermion or boson, from the cross-covariance. However, this is not true for arbitrary noise sources or reservoirs in the non-degenerate limit. For example, a single-photon turnstile device is an engineered source of quiet, single-file photons [32]. An HBT-type measurement of this source would yield a *negative* cross-covariance since the source is quiet, *i.e.*, $F_1 = 0$. To determine directly the statistical nature of quantum particles, one should investigate the two-particle contributions to the noise. Such terms arise in the collision of particles [3, 19].

The symmetrization postulate for quantum particles can lead to non-classical interferences affecting the collision of two quantum particles at a beamsplitter [25, 26]. In figures 2a and 2b, the two-particle scattering amplitudes are calculated for two identical particles from different inputs incident on a $T = 0.5$ beamsplitter. In figure 2a, the detection of one particle in each output, the anti-bunched (1,1) state, is analyzed. The "direct" term interferes quantum mechanically with the physically indistinguishable

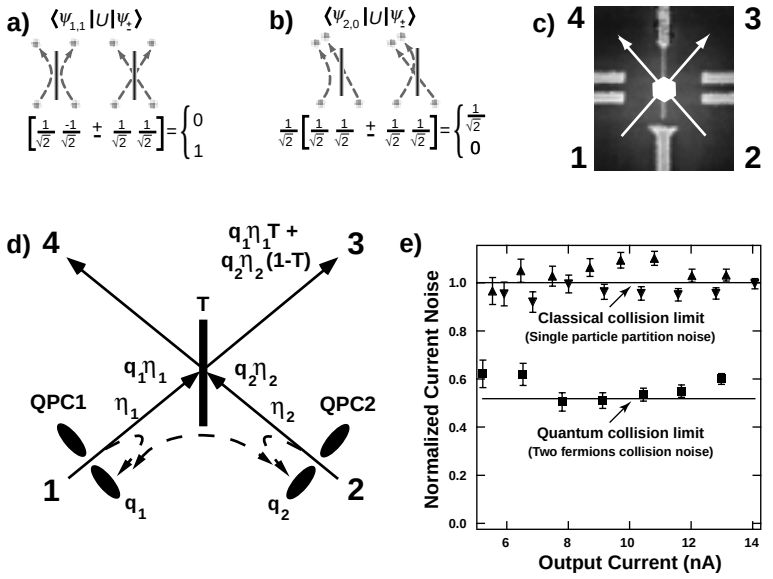

Figure 2. a-b) Quantum interference in the two-particle scattering amplitudes. The input two-particle bosonic (+) or fermionic (−) wavefunction, $|\psi_{\pm}\rangle$, is scattered by the beam splitter's unitary transformation, U, and projected onto the measurement outcome of a) one particle in each output ($|\psi_{1,1}\rangle$), or b) two particles in an output ($|\psi_{2,0}\rangle$). c) Device used for electron collision experiment. Arrows indicate electron entry, collision, and partitioning at the electron beamsplitter. d) Probability model for electron collision. q_1, q_2 are the QPC transmission probabilities, η_1, η_2 account for device non-idealities, and T is the beamsplitter transmission probability. e) Normalized current noise as a function of the output current. Triangles represent the noise when either input is biased alone. The theoretically expected fermionic collision noise based on the transmissions (lower solid line) agrees well with the measured electron collision noise (squares).

"exchange" term in which the roles of the particles are reversed. This interference is destructive for bosons and constructive for fermions. The analgous calculation for two particles in a single output, the bunched (2,0) state, is shown in figure 2b. In contrast, two classical particles would independently scatter into a statistical mixture of the anti-bunched and bunched outputs. In all three cases, the average particle flux at an output is one. However, the Fano factor after collision distinguishes the three cases: $F_3 = 1/2$ for classical particles, $F_3 = 1$ for bosons, and $F_3 = 0$ for fermions.

The device and corresponding model for the electron collision experiment are shown in figures 2c and 2d. Quantum point contacts at the inputs are biased at unity transmission probability, $q_1 = q_2 = 1$, to supply quiet streams of identical particles to the beamsplitter. Non-idealities, such as coherent back-reflection and loss to the opposite inputs, are characterized by η_1 and η_2, and one can use conditional probability arguments to ac-

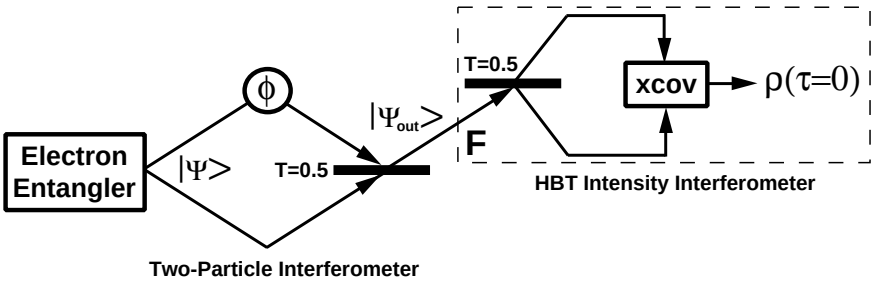

Figure 3. Proposed electron bunching and anti-bunching experiment. A two-electron entangler emits electrons in the spin-singlet state into a two-particle interferometer. A phase shift, ϕ, is applied to spin down electrons in the upper arm. The output Fano factor after collision is measured using an HBT-type intensity interferometer.

count for the quantum mechanical interactions at the beam splitter. To characterize the noise at an output after collision, we use the output Fano factor of a single-particle partition noise experiment (single-sided input experiment). This is because the output of a single-particle partition noise experiment has the same statistics as the output of a collision experiment using classical particles. The output Fano factor in the electron collision case normalized by the output Fano factor for the single-particle partition (classical collision) case is

$$\frac{F_{electron}}{F_{classical}} = \frac{1 - q\eta}{1 - q\eta T} \tag{3}$$

where it is assumed for simplicity that $q_1 = q_2 \equiv q$, $\eta_1 = \eta_2 \equiv \eta$, and the beamsplitter behaves identically as seen from each input. The experimental results are shown in figure 2e. The normalized Fano factor in the collision case is approximately 0.56, representing a significant noise reduction compared with the single-particle partition (classical collision) case. With $q_1 = q_2 = 1$, $T = 1/2$, and using $\eta_1 \approx \eta_2 \approx 0.65$ (as measured independently), the simple model predicts a normalized Fano factor of 0.52, in good agreement with the experimental results. It should be noted that in the dissipative transport limit, partition noise suppression and the recovery of the generalized Johnson-Nyquist noise is due to the frequent elastic/inelastic scattering of electrons and the Pauli exclusion principle [33].

5. Electron Entanglement

The HBT and collision experiments can be used as tools to investigate fundamental quantum mechanics, for example to characterize entangled states and to test Bell's inequality [22]. Here we consider an electron "bunching"

and "anti-bunching" experiment utilizing electrons entangled in specific spin-singlet Bell's states. [22–24]. As shown in figure 3, we assume the existence of an electron entangler, which emits electrons in the following Bell's state into a two-particle interferometer:

$$|\Psi\rangle = \frac{1}{2}\left(|L_1U_2\rangle + |U_1L_2\rangle\right) \otimes \left(|\uparrow_1\downarrow_2\rangle - |\downarrow_1\uparrow_2\rangle\right), \tag{4}$$

where 1 and 2 denote the particle label, L and U denote the spatial wavefunctions with translation to the lower and upper arms of the interferometer, and $\uparrow$ and $\downarrow$ are spins up and down. The spatial wavefunction is symmetric and the spin wavefunction is anti-symmetric, making the total wave function, $|\Psi\rangle$, anti-symmetric under particle exchange as it must be for electrons. We now assume a means to phase shift selectively any spin-down electron which passes through the upper arm. The electrons are then collided at a $T = 0.5$ beamsplitter to yield the following output state:

$$\begin{aligned} |\Psi_{out}\rangle \;\; = \;\; & \frac{1}{4}[-i(e^{i\phi}+1)(|L_1L_2\rangle + |U_1U_2\rangle) \otimes (|\uparrow_1\downarrow_2\rangle - |\downarrow_1\uparrow_2\rangle) + \\ & (e^{i\phi}-1)(|L_1U_2\rangle - |U_1L_2\rangle) \otimes (|\uparrow_1\downarrow_2\rangle + |\downarrow_1\uparrow_2\rangle)]. \end{aligned} \tag{5}$$

The two-electron output can be shifted from bunching ($|L_1L_2\rangle$ and $|U_1U_2\rangle$) to anti-bunching ($|L_1U_2\rangle$ and $|U_1L_2\rangle$) states as a function of ϕ. The Fano factor at either output as a function of ϕ is

$$F(\phi) = \frac{1+\rho(\tau=0,\phi)}{1-\rho(\tau=0,\phi)} = \frac{1}{2}(1+\cos\phi), \tag{6}$$

and can be measured using HBT-type intensity interferometry. Note that two-particle bunching corresponds to $F = 1$ (twice the Fano factor of classical partition noise, $F = 1/2$), while anti-bunching corresponds to $F = 0$. Conditional probability models like those used in sections 3 and 4 can be used to characterize the non-idealities in the electron entangler, collision, and HBT stages.

6. Summary

We presented two quantum electron optics experiments, intensity interferometry and electron collision, and proposed a test of electron entanglement based on these techniques. Investigating quantum optical effects in mesoscopic systems will lead to a more fundamental understanding of the quantum statistics and quantum mechanics of electrons, as well as particles in other systems, for example, the composite particles in the fractional quantum Hall regime [17, 18], Cooper pairs in superconductors [34, 35], and excitons in semiconductors [36].

References

1. C. W. J. Beenakker and H. van Houten, *Solid State Physics vol. 44*, Academic Press, San Diego (1991).
2. R. Hanbury Brown and R. Q. Twiss, Nature **178**, 1447 (1956).
3. C. K. Hong *et al.*, Phys. Rev. Lett. **59**, 2044 (1987).
4. A. Einstein *et al.*, Phys. Rev. **47**, 777 (1935).
5. N. Bohr and L. Rosenfeld, Phys. Rev. **48**, 669 (1938).
6. D. Bohm, *Quantum Theory*, Constable, London (1954).
7. J. S. Bell, Physics **1**, 195 (1964).
8. A. Aspect *et al.*, Phys. Rev. Lett. **47**, 460 (1981).
9. G. Weihs *et al.*, Phys. Rev. Lett. **81**, 5039 (1998).
10. P. Grangier *et al.*, Nature **396**, 537 (1998).
11. G. Nogues *et al.*, Nature **400**, 239 (1999).
12. D. Bouwmeester *et al.*, Nature **390**, 575 (1997).
13. D. Boschi *et al.*, Phys. Rev. Lett. **80**, 1121 (1998).
14. A. Furusawa *et al.*, Science **282**, 706 (1998).
15. M. Reznikov *et al.*, Phys. Rev. Lett. **75**, 3340 (1995).
16. A. Kumar *et al.*, Phys. Rev. Lett. **76**, 2778 (1996).
17. L. Saminadayar *et al.*, Phys. Rev. Lett. **79**, 2526 (1997).
18. R. de Picciotto *et al.*, Nature **389**, 162 (1997).
19. R. C. Liu *et al.*, Nature **391**, 263 (1998).
20. M. Henny *et al.*, Science **284**, 296 (1999).
21. W. D. Oliver *et al.*, Science **284**, 299 (1999).
22. X. Maître *et al.*, to be published in Physica E: Low Dim. Sys. and Nanostruct.
23. M. Michler *et al.*, Phys. Rev. A **53**, R1209 (1996).
24. G. Burkard *et al.*, cond-mat/9906071 (1999).
25. M. Büttiker, Phys. Rev. B **54**, 12485 (1992).
26. T. Martin and R. Landauer, Phys. Rev. B **45**, 1742 (1992).
27. E. M. Purcell, Nature **178**, 1449 (1956).
28. R. E. Burgess, Discussions of the Faraday Society **28**, 151 (1959).
29. G. A. Rebka, Jr. *et al.*, Nature **180**, 1035 (1957).
30. H. J. Kimble *et al.* Phys. Rev. Lett. **39**, 691 (1977).
31. F. Diedrich and H. Walther, Phys. Rev. Lett. **58**, 203 (1987).
32. J. Kim *et al.*, Nature **397**, 500 (1999).
33. R. C. Liu and Y. Yamamoto, Phys. Rev. B **50**, 17411 (1994).
34. J. C. Cuevas *et al.*, Phys. Rev. Lett. **82**, 4086 (1999).
35. J. Torrès and Th. Martin, cond-mat/9906012 (1999).
36. A. Imamoğlu and R. J. Ram, Phys. Lett. A **214**, 193 (1996).
37. The authors gratefully acknowledge S. Machida for his contributions to the cross-correlation circuit, S. Tarucha for his contributions to the beam-splitter device, and support from the Quantum Entanglement Project (ICORP, JST), MURI, and JSEP. W. D. O. gratefully acknowledges additional support from MURI and the NDSEG Fellowship Program.